JOURNAL OF PROPULSION AND POWER
Vol. 14, No. 1, January–February 1998

Method for Noise Suppressing Nozzle Calculation and First Results of Its Implementation

S. Bosniakov,* S. Fonov,† V. Jitenev,‡ A. Shenkin,§ V. Vlasenko,¶ and N. Yatskevich¶
Central Aerohydrodynamic Institute (TsAGI), Moscow 140160, Russia

A description of the method for the flowfield in the noise suppressing nozzle calculation is presented. The method is formulated for the Favre-averaged Navier–Stokes equations. It is based on an explicit monotone second-order approximation, Godunov-type numerical scheme. The first set of calculations is made without turbulent and molecular viscosity being taken into account and shows that the Euler approach allows the main features of the complicated flow in the mixer–ejector nozzle to be described. Special experiments confirm this idea and make the exactness of computational fluid dynamics results more clear.

Nomenclature

a	= speed of sound
C_{fg}	= nozzle gross thrust coefficient, F_g/F_i
$\boldsymbol{F}_k^{\text{conv}}$	= flux of $\boldsymbol{u}$ along x_k axis because of convection and its approximation, $k = 1, 2, 3$
$\boldsymbol{F}_k^{\text{diff}}$	= flux of $\boldsymbol{u}$ aong x_k axis because of molecular and turbulent diffusion and its approximation
F_g	= nozzle gross thrust
F_i	= ideal nozzle gross thrust
K_k	= fluxes of turbulence kinetic energy because of molecular and turbulent diffusion
k_q, k_ω	= coefficients of q, ω molecular transport
NPR	= nozzle pressure ratio, $p_{t,n}/p_a$
$\boldsymbol{n}$	= unit vector of outer normal to the cell boundary
p	= static pressure
p_a	= ambient pressure
$p_{t,j}$	= jet total pressure
$p_{t,n}$	= average total pressure at the nozzle entry
p_w	= wall static pressure
$\boldsymbol{Q}^{\text{conv}}$	= contribution of convection in the equation for $\boldsymbol{u}_{i,j,k}^{n+1}$
$\boldsymbol{Q}^{\text{diff}}$	= contribution of diffusion (including the viscosity and turbulence effects) in the equation for $\boldsymbol{u}_{i,j,k}^{n+1}$
$\boldsymbol{Q}^{\text{source}}$	= contribution of source terms in the equation for $\boldsymbol{u}_{i,j,k}^{n+1}$
q	= intensity of velocity fluctuations
q_k	= heat flux caused by molecular heat conductivity
$\tilde{R}_{ik}$	= Reynolds stresses
$\boldsymbol{r}$	= position vector of (x, y, z) point, $(x, y, z)^T$
S	= cell boundary area
$S(q)$, $S(\omega)$	= source terms in equations for turbulence parameters (q, ω)
T	= temperature
$T_k(q)$, $T_k(\omega)$	= fluxes of q, ω because of molecular and turbulent diffusion
t	= time
$\boldsymbol{u}$	= vector of conservative variables
u_i	= three components of velocity vector, $(i = 1, 2, 3)$ u, v, w
V_{ijk}	= volume of (i, j, k) cell
$\boldsymbol{W}$	= source term in basic equations
x_k	= Caresian coordinates, $(k = 1, 2, 3)$ x, y, z
$1 - C_{fg}$	= nozzle thrust losses
γ	= specific heat ratio
δ_{ik}	= Kronecker delta
ε	= gas total energy per unit of volume
μ	= dynamic coefficient of molecular viscosity
μ_t	= dynamic coefficient of turbulent viscosity
ξ, ν, ζ	= curvilinear coordinates associated with computational cell
ρ	= density
σ_k	= turbulent heat fluxes
τ	= time step
τ_{ik}	= components of viscous stress tensor
ω	= relative dissipation rate of turbulence kinetic energy

Subscripts

i, j, k	= cell centers numeration
$(i \pm 1/2, j, k)$	= cell boundaries numeration
L, R	= states of gas left and right to discontinuity

Superscripts

n	= time step number
$*$	= predictor parameters at $(n + 1)$ time layer
$-$	= Reynolds averaging
$\sim$	= Favre averaging

I. Introduction

THE development of an exhaust system for future supersonic-transport aircraft is closely connected with jet noise reduction. One of the ways to solve this problem assumes the use of an ejector nozzle, in which noise suppression effect is partly achieved by mixing a high-speed jet with ambient air. Experimental investigation of the thrust and acoustic characteristics of a noise-suppressing nozzle (NSN) is a rather difficult task, because of insufficient information about local flow parameters in the mixing zone. Therefore it is necessary to combine wind-tunnel tests with numerical simulation. It is assumed that numerical simulation of flow in NSN ducts will be performed in three stages.

Received Dec. 5, 1996; revision received June 29, 1997; accepted for publication July 10, 1997.

*Head of CFD Group, Propulsion Department, Zhukovsky-3.
†Head of Optical Group.
‡Head Engineer.
§Engineer.
¶Senior Researcher.

Stage I, inviscid computations: A full three-dimensional Euler equation system for inviscid compressible perfect gas is used.

Stage II, turbulent computations without wall effects being taken into account: A full three-dimensional Favre-averaged Euler equation system for inviscid compressible perfect gas is used.

Stage III, turbulent viscous computations with wall effects taken into account: A full three-dimensional Favre-averaged Navier–Stokes equation system is used.

The objective of the stage I computations is to obtain preliminary information about nozzle flow structure and nozzle characteristics. At stages II and III, comparison of these results with those obtained with turbulent and viscous effects allows one to evaluate the viscosity and turbulence contribution to NSN integral and acoustic characteristics.

In this paper, we publish the numerical method for all stages of investigations, describe the procedure of grid generation, and discuss the results of inviscid calculations (stage I). Experimental data are used for the computational fluid dynamics (CFD) result verification.

II. Basic Equations

The NSN flow computation is performed with the use of a time-marching procedure. In this case, some initial flowfield is given and the stationary flow is considered as the limit of flowfield nonstationary adaptation to given stationary boundary conditions. Therefore, the nonstationary basic equations are used.

The full three-dimensional Favre-averaged Navier–Stokes equation system for perfect gas[1] may be written in the following conservative form (the summing over repeating indexes is assumed):

$$\frac{\partial \boldsymbol{u}}{\partial t} + \frac{\partial(\boldsymbol{F}_k^{\text{conv}} + \boldsymbol{F}_k^{\text{diff}})}{\partial x_k} = \boldsymbol{W} \tag{1}$$

In this equation

$$\boldsymbol{u} = [\bar{\rho},\ \bar{\rho}\tilde{u}_i,\ \bar{\varepsilon},\ \bar{\rho}q,\ \bar{\rho}\omega]^T \tag{2}$$

$$\boldsymbol{F}_k^{\text{conv}} = \begin{bmatrix} \bar{\rho}\tilde{u}_k \\ \bar{\rho}\tilde{u}_i\tilde{u}_k + \bar{p}\delta_{ik} \\ (\bar{\varepsilon} + \bar{p})\tilde{u}_k \\ \bar{\rho}q\tilde{u}_k \\ \bar{\rho}\omega\tilde{u}_k \end{bmatrix} \tag{3}$$

$$\boldsymbol{F}_k^{\text{diff}} = \begin{bmatrix} 0 \\ \bar{\rho}\tilde{R}_{ik} - \bar{\tau}_{ik} \\ (\bar{\rho}\tilde{R}_{ik} - \bar{\tau}_{ik})\tilde{u}_i + (\bar{\rho}\tilde{\sigma}_k - \tilde{q}_k) + K_k \\ T(q)_k \\ T(\omega)_k \end{bmatrix} \tag{4}$$

$$\boldsymbol{W} = [0,\ 0,\ 0,\ S(q),\ S(\omega)]^T$$

For the closure of equation system (1), we use a gas law, an expression for gas total energy, an expression for gas internal energy per unit of mass (it is approximated by quadratic function of temperature), an expression for viscous stress tensor components, the Sutherland formula for molecular viscosity coefficient, and expressions for heat fluxes caused by molecular heat conductivity.

The turbulence effects are taken into account by using the $(q - \omega)$ model of turbulence.[2] The Dash model[3] is used to describe the effects of turbulence compressibility.

To receive an Euler equation system from Eq. (1), it is necessary to omit the $\boldsymbol{F}_k^{\text{diff}}$ and $\boldsymbol{W}$ terms, and to exclude the two last equations for turbulence parameters. Favre-averaged Euler equations can be obtained by omitting the viscous terms, $\bar{\tau}_{ik}$ and $\tilde{q}_k$, in Eq. (4).

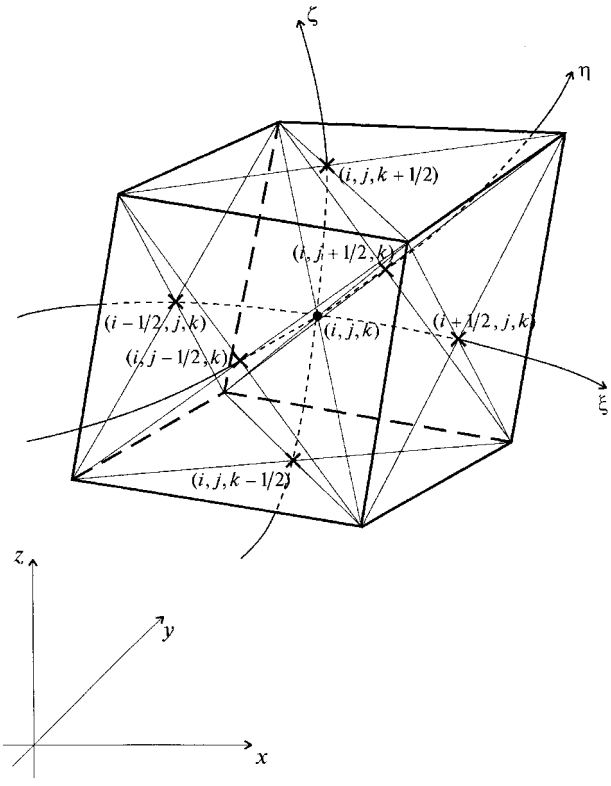

Fig. 1 Computational cell and map of indexes.

III. Description of Numerical Method

A. General Formulation of Difference Scheme

The approximation of Eq. (1) is performed using a finite volume approach to the numerical scheme construction. The computational domain is covered by the nonchangeable grid. The numeration of cell centers and cell boundaries is illustrated in Fig. 1.

The numerical scheme may be written in the following form:

$$\boldsymbol{u}_{ijk}^{n+1} = \boldsymbol{u}_{ijk}^{n} + \frac{\tau}{V_{ijk}}(\boldsymbol{Q}^{\text{conv}} + \boldsymbol{Q}^{\text{diff}} + \boldsymbol{Q}^{\text{source}}) \tag{5}$$

$\boldsymbol{u}_{ijk}^{n}$ approximates the value of integral

$$\frac{1}{V_{ijk}} \int_{V_{ijk}} \boldsymbol{u}(\boldsymbol{r}, t_n)\, \mathrm{d}\boldsymbol{r}$$

$\boldsymbol{Q}^{\text{conv}}$ and $\boldsymbol{Q}^{\text{diff}}$ may be written as follows:

$$\boldsymbol{Q}^{\text{conv}} = -(\Delta_i + \Delta_j + \Delta_k)[\boldsymbol{F}^{\text{conv}} \cdot S_l]$$

$$\boldsymbol{Q}^{\text{diff}} = -(\Delta_i + \Delta_j + \Delta_k)[\boldsymbol{F}^{\text{diff}} \cdot S_l]$$

Δ_i, Δ_j, and Δ_k are difference operators; for example,

$$\Delta_i a = a_{i+1/2,j,k} - a_{i-1/2,j,k}$$

$\boldsymbol{S}$ is the vector of the cell boundary area

$$\boldsymbol{S} = (S_x,\ S_y,\ S_z)^T = S \cdot \boldsymbol{n}$$

$\boldsymbol{F}_l^{\text{conv}}$, $\boldsymbol{F}_l^{\text{diff}}$ (l = 1, 2, 3) are approximations of corresponding physical fluxes

$$\boldsymbol{F}_l^{\text{conv}} \approx \frac{1}{S\cdot\tau}\cdot\int_{t_n}^{t_{n+1}} \mathrm{d}t \int_S \boldsymbol{F}_l^{\text{conv}}(\boldsymbol{r}, t)\,\mathrm{d}S$$
$$\boldsymbol{F}_l^{\text{diff}} \approx \frac{1}{S\cdot\tau}\cdot\int_{t_n}^{t_{n+1}} \mathrm{d}t \int_S \boldsymbol{F}_l^{\text{diff}}(\boldsymbol{r}, t)\,\mathrm{d}S \tag{6}$$

$\boldsymbol{Q}^{\text{source}}$ approximates source terms in Eq. (1):

$$\boldsymbol{Q}^{\text{source}} \approx \frac{1}{\tau}\cdot\int_{t_n}^{t_{n+1}} \mathrm{d}t \int_{V_{ijk}} \boldsymbol{W}(\boldsymbol{r}, t)\,\mathrm{d}\boldsymbol{r}$$

The concrete difference scheme is determined by the approach to the preceding integrals' approximation.

B. Approximation of Convective Fluxes

The Godunov-Kolgan-Rodionov (GKR) scheme[4–7] is chosen to describe the convection. This scheme belongs to the class of Godunov-type schemes and has the second order of accuracy, both in space and in time. The convective flux in Eqs. (6) is calculated as follows:

$$(\boldsymbol{F}_l^{\text{conv}})_{i+1/2,j,k} = \boldsymbol{F}_l^{\text{conv}}(\boldsymbol{U}_{i+1/2,j,k})$$

where $\boldsymbol{F}_l^{\text{conv}}(\boldsymbol{u})$ is real physical function, in which approximate values of gas parameters at a given cell boundary are substituted. These parameters are found by solving the Riemann problem about the decay of arbitrary discontinuity between two semi-infinite uniform inviscid flows:

$$\boldsymbol{U}_{i+1/2,j,k} = \boldsymbol{U}(\boldsymbol{u}_L, \boldsymbol{u}_R) \tag{7}$$

where the L index corresponds to the flow left to (i + 1/2, j, k) boundary [(i, j, k) cell], and the R index corresponds to the flow right to (i + 1/2, j, k) boundary [(i + 1, j, k) cell].

The clear physical sense of each action provides the high reliability and quality of the results. We use the original nonlinearized iterative solution of the Riemann problem, taking into account the gas thermodynamic properties' dependence upon temperature. The special features of the algorithm are as follows.

1) The exact relations for gas parameters' calculation before and after the shock wave: Gas thermodynamic properties' dependence upon temperature is taken into account.

2) The approximate relations for gas parameters' variation in the expansion wave: These relations are received for the gas with thermodynamic properties, depending upon the temperature. In this case, it's impossible to integrate differential equations for Riemann invariants. The different procedures for calculations inside and outside of the wave are used.

a) To determine the gas parameters before and after the expansion wave, the formulas for ideal gas are implemented. The average value of specific heats' ratio is substituted in these formulas.

b) To determine the gas parameters inside the expansion wave, the more complicated procedure is used. It modifies the known values that are constant for ideal gas but are non-constant in reality. Namely, in the case of an ideal gas, the following values are constant through the expansion wave:

$$\gamma, \qquad V - \frac{2c}{\gamma - 1}\cdot s, \qquad \frac{p}{\rho^\gamma}$$

V is the gas velocity in the one-dimensional flow through the expansion wave, c is speed of sound, and s = 1 (−1) is the expansion wave propagating to the right (left) from the discontinuity.

To take into account the gas thermodynamic properties' dependence upon temperature, it is assumed that these values vary linearly with the characteristics' inclination angle in the expansion wave. This assumption guarantees the continuity of the parameters' variation across the expansion wave. In addition, the resulting approximate relations for the gas parameters inside the expansion wave become exact when the ideal gas with constant heat ratio is considered.

3) Double-step solution of the Riemann problem in the case of iteration divergence: As a rule, iteration divergence takes place if the Riemann problem solution includes two intensive expansion waves or if vacuum is realized. To avoid this divergence, it is assumed that both waves in the Riemann task are continuous. In this situation, there is an analytical solution for an ideal gas with a constant specific heat ratio.[4] At the first step, these analytical formulas with an average value of γ are used. The second step takes into account the variation of γ. This approach allows one to achieve an almost exact solution and to avoid the problem of divergence.

To provide the second-order approximation in space coordinates, the parameter distribution is supposed to be linear in every computational cell. The parameter gradients are determined in every cell with the use of a minimum derivative value principle (MDVP). This principle was proposed by Kolgan.[5] Later, the analogous method was proposed and founded mathematically by Harten.[8] The total variation diminishing (TVD) approach[8] widely used today is the analogue of approach[5] that is used in this paper.

The primary formulation of MDVP for irregular grids[9] sometimes leads to nonphysical values of $\boldsymbol{u}_L$ and $\boldsymbol{u}_R$ [see Eq. (7)], under the circumstances of strong grid nonuniformity. In this paper, the new approach is proposed to overcome this problem. MDVP is formulated using a curvilinear coordinate system, connected with grid lines.

Let us consider the curvilinear frame (ξ, η, ζ) with coordinate lines across the cell centers and the cell boundaries' centers (Fig. 1). Parameters of flows for the Riemann problem solution [see Eq. (7)] are determined as follows:

$$f_L = f_{i,j,k} + \left(\frac{\partial f}{\partial \xi}\right)_{i,j,k}\cdot\Delta_L\xi$$
$$f_R = f_{i,j,k} + \left(\frac{\partial f}{\partial \xi}\right)_{i+1,j,k}\cdot\Delta_R\xi \tag{8}$$

$$f = p, \rho, u, v, w, q, \omega$$
$$\Delta_L\xi = |\boldsymbol{r}_{i+1/2,j,k} - \boldsymbol{r}_{i,j,k}|$$
$$\Delta_R\xi = -|\boldsymbol{r}_{i+1,j,k} - \boldsymbol{r}_{i+1/2,j,k}|$$
$$\left(\frac{\partial f}{\partial \xi}\right)_{i,j,k} = \text{minmod}\left(\frac{\Delta_{i-1/2}f^n}{\Delta_{i-1/2}\xi}, \frac{\Delta_{i+1/2}f^n}{\Delta_{i+1/2}\xi}\right) \tag{9}$$
$$\text{minmod}(a, b) = \frac{\text{sign } a + \text{sign } b}{2}\min(|a|, |b|)$$
$$\Delta_{i+1/2}f^n = f^n_{i+1,j,k} - f^n_{i,j,k}$$
$$\Delta_{i+1/2}\xi = \Delta_L\xi + \Delta_R\xi$$

This approximation of derivatives works well if flows with a primary direction of parameters variation are simulated (mixing layers, jets, boundary layers). In fact, it is assumed that parameters vary monotonically between the centers of neighboring cells. This assumption may fail if strongly curved grids without adaptation to flow structure are considered. In this work, the approach to grid generation allows one to obtain almost regular grids with the resolution of the main flow features.

To obtain the second-order approximation in time, the modification of approach proposed by Rodionov[6,7] is used. It is a double-step procedure.

The first step is predictor: It is used to receive the initial approximation to parameters at the $(n + 1)$ time layer, f^*_{ijk}. Equation (8) is used with $f_{i,j,k} = f^n_{i,j,k}$.

The second step is corrector: It is used to receive the final values of gas parameters at the $(n + 1)$ time layer, f^{n+1}_{ijk}. Equation (8) is used with $f_{i,j,k} = 0.5 \cdot (f^n_{i,j,k} + f^*_{i,j,k})$. It is necessary to note that $(\partial f/\partial\xi)_{i,j,k}$, $(\partial f/\partial\xi)_{i+1,j,k}$ are calculated with the implementation of explicit time layer n parameters [see Eq. (9)].

The GKR scheme is stable if the standard Courant–Friedrichs–Lewy (CFL) limitation[4] for the time step is satisfied.

C. Approximation of Viscous and Turbulent Fluxes

For the calculation of diffusion fluxes, the modification of central-difference derivatives' approximation is used.

In the first step, in each cell center, the derivatives along the axes (Fig. 1) are calculated with the use of linear interpolation of derivative-oriented approximations; for example,

$$\left(\frac{\partial f}{\partial \xi}\right)_{i,j,k} = \frac{\Delta_{i+1/2}\xi \cdot \dfrac{\Delta_{i-1/2} f}{\Delta_{i-1/2}\xi} + \Delta_{i-1/2}\xi \cdot \dfrac{\Delta_{i+1/2} f}{\Delta_{i+1/2}\xi}}{\Delta_{i-1/2}\xi + \Delta_{i+1/2}\xi} \tag{10}$$

$(\partial f/\partial\eta)_{i,j,k}$ and $(\partial f/\partial\zeta)_{i,j,k}$ are determined in the same way.

The test calculations of turbulent flows show that the central-difference approximation [Eq. (10)] sometimes leads to the appearance of nonphysical oscillations in the solution. To smooth these oscillations, the approximation order must be lowered. When $\Delta_{i-1/2} f \cdot \Delta_{i+1/2} f < 0$, it is assumed that $(\partial f/\partial\xi)_{i,j,k} = 0$. This modification guarantees the scheme stability.

In the second step, derivatives for cell boundaries are determined. For example, let's consider the boundary $(i + 1/2, j, k)$:

$$\left(\frac{\partial f}{\partial \xi}\right)_{i+1/2,j,k} = \frac{\Delta_{i+1/2} f - \dfrac{1}{2} \cdot \Delta_{i+1/2} \left(\dfrac{\partial f}{\partial \xi}\right) \cdot (\Delta_R \xi - \Delta_L \xi)}{\Delta_{i+1/2}\xi}$$

$$\left(\frac{\partial f}{\partial \eta}\right)_{i+1/2,j,k} = \frac{\Delta_R \xi \cdot \left(\dfrac{\partial f}{\partial \eta}\right)_{i,j,k} + \Delta_L \xi \cdot \left(\dfrac{\partial f}{\partial \eta}\right)_{i+1,j,k}}{\Delta_{i+1/2}\xi}$$

$$\left(\frac{\partial f}{\partial \zeta}\right)_{i+1/2,j,k} = \frac{\Delta_R \xi \cdot \left(\dfrac{\partial f}{\partial \zeta}\right)_{i,j,k} + \Delta_L \xi \cdot \left(\dfrac{\partial f}{\partial \zeta}\right)_{i+1,j,k}}{\Delta_{i+1/2}\xi}$$

Finally, $(\partial f/\partial\xi)$, $(\partial f/\partial\eta)$, and $(\partial f/\partial\zeta)$ are converted to $(\partial f/\partial x)$, $(\partial f/\partial y)$, and $(\partial f/\partial z)$, respectively.

Contrary to the method of derivatives determination in the Rodionov scheme, for the second-order approximation of diffusion fluxes, it is necessary to recalculate derivatives at the corrector step. At the predictor step, derivatives in diffusion terms are calculated with the use of parameters at the explicit time layer, $f^n_{i,j,k}$, and at the corrector step, with the use of parameters at the time layer $(n + 1/2) - 0.5 \cdot (f^n_{i,j,k} + f^{n+1}_{i,j,k})$.

This approximation of diffusion terms produces the following time-step limitation:

$$\tau \le \tau^{\text{diff}} = (1/\tau_i + 1/\tau_j + 1/\tau_k)^{-1}$$

where, for example, τ_i is determined by the following formula:

$$\tau_i = 0.5 \cdot \frac{\rho^n_{i,j,k} \cdot |A_{i-1/2} A_{i+1/2}|^2}{\mu^n_{i,j,k} + (\mu_t)^n_{i,j,k}}$$

$|A_{i-1/2} A_{i+1/2}|$ is the distance between the centers of $(i - 1/2, j, k)$ and $(i + 1/2, j, k)$ boundaries.

D. Approximation of Source Terms

Equation (1) is stiff because of the presence of the source terms.[10] Therefore, the point-implicit approach is used for the approximation of basic equations. In this approach, space effects contributions $\boldsymbol{Q}^{\text{conv}}$, $\boldsymbol{Q}^{\text{diff}}$ [see Eq. (5)] are approximated using parameters at the explicit layer t_n. For $\boldsymbol{Q}^{\text{source}}$, the semi-implicit approximation with the second-order accuracy in time is used (see also Sec. II.A)

$$\boldsymbol{Q}^{\text{source}} = \frac{\boldsymbol{W}^n_{i,j,k} + \boldsymbol{W}^{n+1}_{i,j,k}}{2} V_{i,j,k}$$

As a result, in every cell, the two last equations in Eq. (5) (for q^{n+1} and ω^{n+1}) form an implicit system. It isn't connected with the neighboring cells. This implicit equation system is solved at the predictor step by the one step of the Newton method, and the $\boldsymbol{W}^*_{i,j,k}$ is calculated.

At the corrector step it's assumed that $\boldsymbol{W}^{n+1}_{i,j,k} = \boldsymbol{W}^*_{i,j,k}$. As a result, the equation system becomes q^{n+1}, and ω^{n+1} becomes explicit. This approach leads to a considerable decrease of calculation time. Because the source terms at the predictor step are calculated with second-order accuracy in time, the accuracy and quality of numerical solution don't degrade.

Time-step limitation produced by source terms approximation is based upon the analysis of $\partial \boldsymbol{W}/\partial \boldsymbol{u}$ matrix eigenvalues, λ_i. Each eigenvalue is connected with a special mode of solution (in the exact solution these modes are approximately proportional to $e^{\lambda_i t}$).[10] The following steps are required:

1) All modes of numerical solution are to be stable.

2) Their behavior (damping or growth in time) is to be the same as the behavior of exact solution modes.

3) The basic modes are to be positive. The term basic modes means that if all modes damp, i.e., all $\lambda_i < 0$, then the basic modes are $\lambda_i \in (2\lambda_{\max}, \lambda_{\max})$, $\lambda_{\max}$ is the maximum eigenvalue; if there are undamping modes ($\lambda_i \ge 0$), they are all treated as basic ones. These requirements lead to the $\tau \le \tau^{\text{source}} = 1/\lambda_{\max}$ limitation.

E. Solution of the Small-Time Step Problem

The flow in the nozzle with noise suppresser includes physical phenomena in a wide range of scales: boundary layers, mixing layers, large-scale gas motions in the mixer, flow in the whole nozzle and in the nozzle jet, and its interaction with outer flow.

The problems caused by the multiscale physical structure of the flowfield are typical both for the Navier–Stokes computations and the Euler tasks. The only problem is the necessity to cover the computational domain by the grid containing the cells allowed to describe all the scales of the task. Usually these scales vary by several orders. The common approach to solving the problem of memory is by using a nonuniform grid. But the problem of the small time step remains, because it is defined by the minimal cells' size.

To solve the small time-step problem in the framework of explicit approach, we have developed a variant of GKR scheme with local time stepping. In this case, the computation in each cell is performed with the time step determined by time-step limitations for this separate cell. As a result, the value of time step differs from one cell to another. But when all parameters $\boldsymbol{u}^{n+1}_{i,j,k}$ are determined, it is assumed that all of these parameters belong to the same time layer. After that this procedure is repeated up to the moment when stationary solution will be achieved. This idea is based upon the following reasons:

1) You can't violate the CFL condition in any cell.

2) Calculating with the global time step, i.e., with the time step determined by the minimal cell, most of the cells are calculated with decreased accuracy. This is explained as follows: the local Courant number Cu is 10–1000 times less than 1, and the numerical viscosity is proportional to $(1 - Cu)$.

3) To provide the convergence of the solution, the disturbances must run through the computational domain several times.

4) The physical velocity of the disturbances' propagation is approximately equal to the speed of sound or to the difference between the speed of sound and the local velocity. It doesn't depend upon the computational grid. Therefore, the physical time necessary for the convergence doesn't depend upon the computational grid. It depends upon the size of computational domain only.

5) The numerical velocity of the disturbances' propagation is proportional to the local Courant number. Therefore, using the local time stepping accelerates the convergence.

During the local time stepping, the parameters on the current calculation step cannot be assigned to the single time level. Moreover, the unsteady process as a whole is described nonphysically. In each separate computational cell, we have a physically correct nonstationary process. And when the steady-state solution is achieved, the time level may be pointed; it is infinity.

The local time-step approach has previously been used in nonmonotone schemes, i.e., the Jameson scheme.[11] Nonphysical oscillations caused by this method have been suppressed by the artificial viscosity and monotonizers built into the schemes of this type. Note that the Jameson scheme was originally intended for transonic regimes only. Authors of the present paper developed a reliable working algorithm suitable for the wide range of Mach numbers. This algorithm has been found to be stable for 1) inviscid multiscale tasks with the strong changes of parameters; 2) viscid laminar two- and three-dimensional flows with the strong changes of parameters, calculated on strongly nonuniform grids; and for 3) flows with turbulent boundary layers, with free turbulence and combustion.

The local time-step approach works well in the computation of flowfield in noise suppressing nozzles.

IV. Mathematical Model of Nozzle Geometry

A mathematical model of nozzle geometry is created in accordance with the plots for the experimental manufacturing model (Fig. 2). It consists of several parts: duct, lobes, ejector, central body, flaps, etc. The surface of each part is approximated with the aid of Coons patches fitted to each other. Grid lines at the surface are continuous during the transition from one patch to another.

The duct of the nozzle is used for the high-pressure air supply. It's made like the tube with a smooth transition from a circular to a rectangular cross section. A mixer with lobes is mounted at the end of this tube. It provides the mixing of the high-pressure air with the outer flow sucked by a jet in the ejector. The ejector is formed with sidewalls and two flaps. The nose part of each flap protrudes into the outer flow and forms the intake with leaps. Flaps have a good contour and there is no separation in the flowover. The central body is made as an insertion with a rhomboid profile. It joins both nozzle and ejector at the lateral inner surface.

For the best approximation, the nozzle geometry is divided into compartments. A compartment is the topologically uniform part of the geometry that permits the construction of a regular computational grid based on it. All compartments are fitted to each other and form the multiblock structure that is used for calculations.

V. Computational Grid

The computational grid in the nozzle is constructed with the use of a multiblock approach. It may be divided into fragments that topologically correspond to cubes. These cubes are named blocks or subregions. The total grid consists of 137 blocks and contains 650,000 cells; approximately 350,000 cells are in the nozzle and 300,000 are in the outer flow. An example of the grid is shown at Fig. 3. It is easy to see that the grid has a regular structure, but somewhere the nonregularity is inevitable. For example, in the case of angular point, the side of the block can degenerate to the line or to the point. Let's consider the nozzle mixer. The grid over the lobes contains irregular blocks because of the lobe's duct angular structure. In the irregular blocks one side degenerates to the line. Moreover, the grid lines near the lobes contain kinks, and the size of neighboring cells can jump from one value to another when you cross the block's frontier. All of these irregularities of the grid are shown at Fig. 3. The nonregular grid disturbs the solution received by the numerical scheme. Experience permits us to say that using a second-order Godunov-type scheme leads to the perfect solution to this problem.

Outer boundaries of the grid are distanced from the surface to remove the influence of boundary conditions to the flow inside the nozzle. This distance is equal to the character length of the task. It can be diminished in the supersonic case, but for the sub- and transonic flow calculations it must be as large as possible. In some cases, the characteristic length is equal to the length of the nozzle.

VI. Facility for Nozzle Model Testing

An experimental investigation of a two-dimensional mixer/ejector nozzle were done in the transonic nozzle test facility of the Ramjet Wind Tunnel (TPD) [in accordance with Central Aerohydrodynamic Institute (TsAGI) classification]. This facility (Fig. 4) was designed exclusively for exhaust model investigations. The diameter of the wind-tunnel test section is equal to 800 mm, the external flow in the range of Mach numbers from 0.3 to 1.0 is provided by an axisymmetric convergent nozzle with a cylinder perforated pipe. Reynolds numbers based on the test section diameter vary from 0.7×10^7 to 1.7×10^7, depending upon the external Mach number. The model in this wind tunnel is mounted at the central sting, which is supported by four struts in the wind tunnel precham-

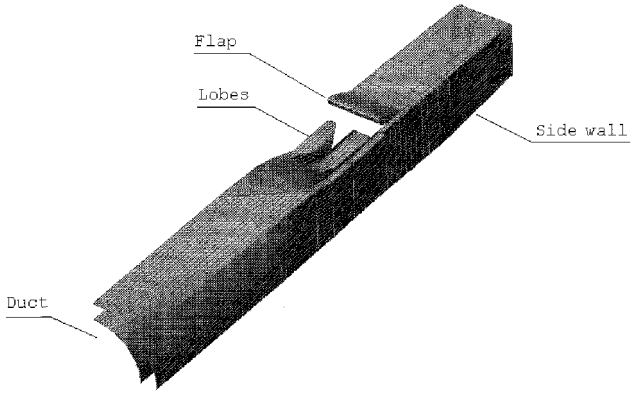

Fig. 2 Mathematical model of nozzle geometry.

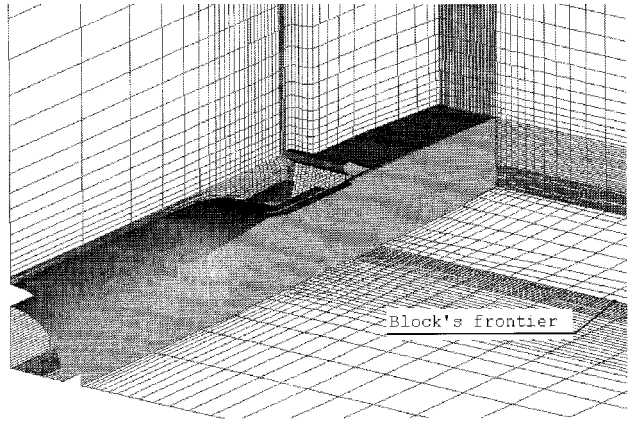

Fig. 3 Multiblock grid around nozzle.

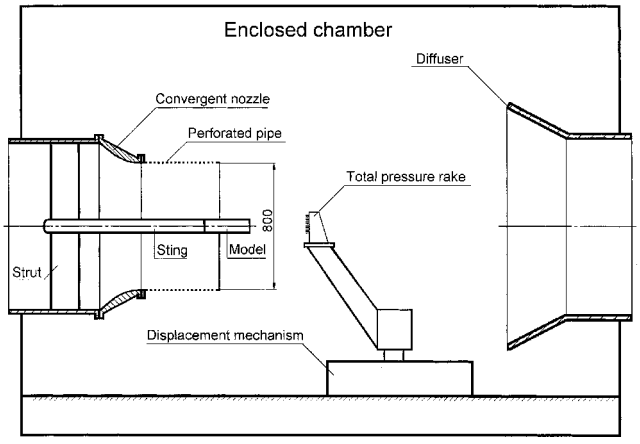

Fig. 4 TPD wind tunnel and model on sting.

ber. Cold compressed air with a stagnation temperature equal to 1 atm is supplied to the nozzle duct through these struts. The mass flow rate of compressed air is measured by a flow meter located outside the wind tunnel.

In this experimental series, all tests are accomplished in an enclosed chamber. The jet and external flow after the model are exhausted to the atmosphere through a diffuser. The model is supported by the axisymmetric sting. The stagnation pressure in the duct before the model is measured by two probes, with an accuracy 0.3% in the $0.05-5 \times 10^5$ Pa range. The average total pressure at the model entry $p_{t,n}$ and discharge coefficient in the nozzle throat are determined by using sonic calibration nozzles. The resultant axial force acting upon the model surface is measured by one-component strain-gauge balances with an accuracy of 0.1% in the 0–0.98 kN range. Data acquisition systems and equipment of the TPD wind tunnel allow the determination of the main nozzle performance with the following accuracy: 1) mass-flow rate, 0.5%; 2) nozzle gross thrust coefficient in static conditions, 0.5%; and 3) nozzle gross thrust coefficient in flight conditions, 0.7%.

Technology of nozzle tests in TsAGI is rather voluminous and complicated. There is no need to discuss the way performance was obtained. In this paper it is enough to say that the nozzle gross thrust coefficient is the ratio of a measured gross thrust to the ideal isentropic one.

Investigations of total pressure inside the exhaust jet behind the model exit section $p_{t,j}$ are carried out by a rake in static conditions. The rake consists of 26 total-pressure tubes. The spacing between neighbor probes is equal to 4 mm. Lateral movement of the rake with a step approximately equal to 2 mm is provided by a remote-controlled mechanism. Total pressure values are measured with an accuracy 0.3% in the $0.05-5 \times 10^5$ Pa range.

VII. Configuration of the Nozzle Experimental Model

The two-dimensional mixer/ejector nozzle is designed for jet noise reduction at takeoff regimes. The primary corrugated nozzle divides the exhaust jet into six parts, thus enlarging its surface. Jets ingest ambient air into the ejector where a mixing process takes place. As a result, the velocity of gas mixing becomes lower and the noise suppression effect is achieved. The two-dimensional mixer/ejector nozzle model is shown in Fig. 5. A tested configuration is developed as a modification of the Societe Nationale d'Etude et de Construction de Moteurs d'Aviation/Central Aerohydrodynamic Institute/Central Institute of Aviation Motors (SNECMA/TsAGI/CIAM) model used for the noise suppression problem investigation.[12] The primary corrugated nozzle has six rectangular lobes. The angle of the nozzle duct convergence is 40 deg. The ratio of the ejector exit area to the primary nozzle throat area is equal to

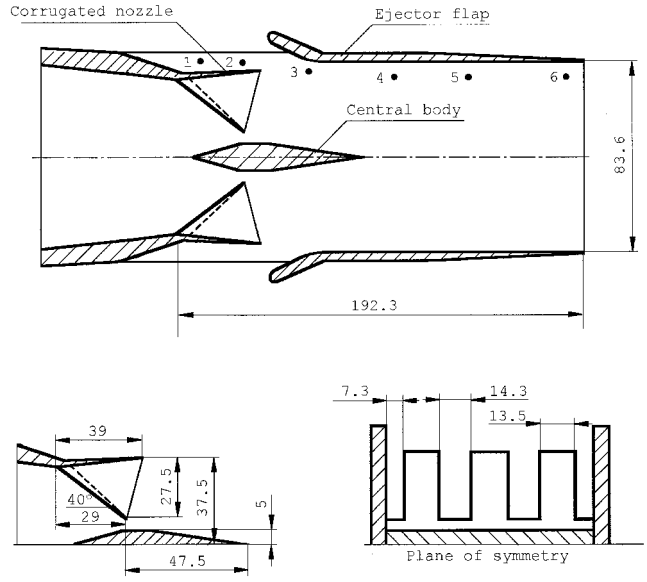

Fig. 5 Sketch of the nozzle model (all dimensions are given in millimeters).

2.34. The construction of the axisymmetric sting provides simultaneous measurement of axial force and pressure on the model surface. Six static pressure orifices are located on the sidewall surface in the ejector duct. An accuracy of wall pressure p_w measurements is 0.3% in the $0.01-2 \times 10^5$ Pa range.

VIII. Optical Methods Used in Experiments

The application of the pressure-sensitive paint method (PSP) is very attractive for the static pressure distributions along sidewall investigations. Measurement accuracy of the PSP is worse compared to the standard technique, but possibility to obtain a pressure field picture on the surface compensates for this disadvantage, especially in the case of a complex structure field.

A general layout of the optical pressure measurement system using PSP is shown on Fig. 6. The PSP is applied as a very thin polymeric layer by spraying on the internal surfaces of the ejector and its cowl, the central body, and external surface of the corrugated nozzle (1). A nitrogen laser (2), having an output power 250 MW, is used as exciting light source. A beam splitter (3) is installed on the laser output, and two fibers (4) and illuminators (5) provide illumination of the appropriate parts of the model. Luminescence fields on the surfaces under study are acquired by a digital charged-coupled device (CCD) camera (6) and broadcast standard CCD camera (7), having an analog video output. An analog CCD camera (7) is only used for video acquisition from the surface of a corrugated nozzle. The sets of the optical filters cutting excitation light and bypassing PSP luminescence are installed on the camera's objective lenses. The signal from the digital CCD camera is transformed by the camera's controller and it is acquired by an image processing system (8), which is based on a personal computer (9). Video output from the analog CCD camera is registered by a standard video recorder (10). The specialized digital image processing system is used for digitizing and preprocessing these records. The resulting information is developed on personal computer-based image processing system (8) and (9). Intensity to pressure field conversions are performed with a dedicated software package, OMS. Of particular interest in this experiment is the registration of the images under small angles to the surfaces, which resulted in significant image distortions. Distortion corrections are performed with the use of a mathematical model of the nozzle shape and with information about the marker positions. These markers are applied in the appropriate points on the model surface in the process of PSP preparation. The markers' coordinates are measured di-

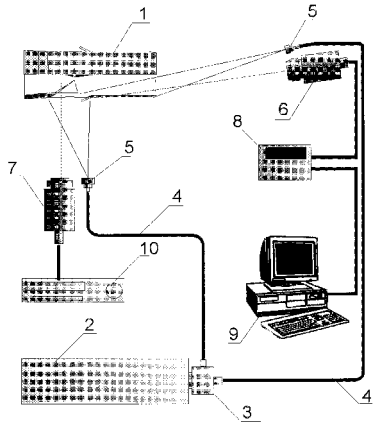

Fig. 6 Tools for the optical experiment.

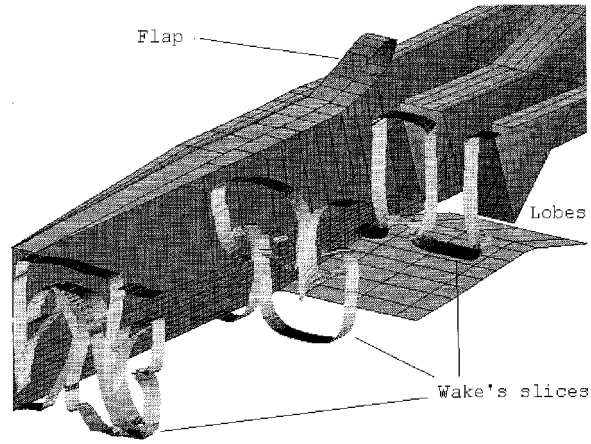

Fig. 7 Wake after the lobes in the mixer.

rectly on the model surface. The resulting pressure fields after the distortion correction procedure are transformed in the nodes of the nets, describing the mathematical model of the appropriate surface under study.

The model is instrumented with standard pressure taps installed in several points of the sidewalls of the mixing chamber (Fig. 5). Pressure taps are connected with the standard pressure gauges. These measurements are used for verification of PSP results.

The light sheet method (smoke screen) is used for investigation of the flowfield structure. An optical scheme realizing this light sheet method is the same as the one shown in Fig. 6.

IX. Results of the Calculations and Experiments

Calculations are made at different values of nozzle pressure ratios and at different Mach numbers for the outer flow. As the first step, the Euler part of the program is used. The main purpose is to investigate the features of the flow in the mixer of the nozzle and to receive the initial information for comparison with the next step of calculations. A subject of great interest is the flow after the lobes. It is a well-known fact[12,13] that the flow in the mixer after the lobes is characterized by numerous vortices that provide and intensify the mixing process. The result by means of calculations is shown in Fig. 7. The lobes, part of the cowl, and the centerbody are clearly seen. Flow after the lobes is visualized as the slices of solids (so-called wake's slices). This result makes the process of vortex formation more clear. The high-pressure flow forces the streamlines to rotate. Rotation is combined with the movement in the side and up directions. It leads to the intersection of the vortices, and the flow after the intersection becomes very complicated. The wake's cross sections are shown at Fig. 8; they confirm the ideas discussed earlier. It's easy to see that the wake surface isn't smooth and contains some picks that create their own picture of interaction. The algorithm of wake surface construction is similar to the Euler method of integrating. For example, if you know the position of a liquid particle and the velocity vector for this particle, you can determinate its position for the next time. The wake constructed by this method isn't stable, which means that some disturbances in the numerical solution are possible. The instability of the Euler algorithm of integrating depends on the time step. The different time steps we used in this case give the same result. Picks (Fig. 8) at the wake surface didn't change the position and intensity. They show that instability is the feature of the wake, but not a mistake of integration; perhaps it's the Kelvin-Helmgoltz phenomenon.[8]

Comparison of CFD and experimental data is shown at Fig. 9. Figure 9a shows a slice of the wake at the exit of the nozzle's mixer, received by means of calculations. Figure 9b is the same wake received by means of a smoke screen during

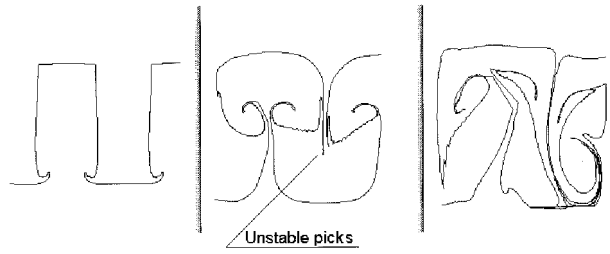

Fig. 8 Cross section of the wake slices.

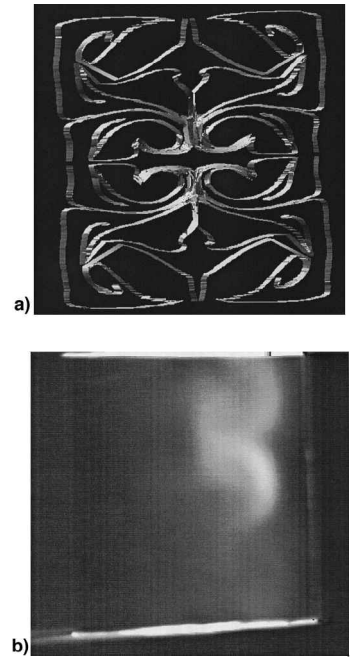

Fig. 9 Comparison of CFD and experimental data at the exit section: a) CFD data and b) smoke screen.

the experiment. Both Figs. 9a and 9b show the boundary that can be interpreted as belonging to the wake. Figure 9a has more detail, but in the main features it's similar to the experimental one. The idea of the experiment is very clear. Smoke propagates along streamlines, and if you place the source of the smoke out of the duct, the smoke is sucked inside of it because of ejection. Thus, you can visualize the process of ejection and receive the shape of the jet boundary after the flows' mixing. In this experiment, only one smoke source is used. Therefore, the upper part of both Figs. 9a and 9b is clear, and the lower part of these figures is in the shadows. In Fig.

9, the flow is symmetrical and the information provided by this was adequate for understanding the whole phenomenon.

Figure 10 demonstrates a comparison of total pressure distribution at the same section (exit of the mixer); a function of nondimensional total pressure $(p_{t,j} - p_a)/(p_{t,n} - p_a)$ was used. The CFD data are depicted as black-white tone distribution. The scale of this distribution is on the right part of the figure. The chart in Fig. 10 shows the values of nondimensional total pressure along the white line in the middle of the picture. The solid inverse line corresponds to CFD data, and markers are the experimental ones. It's easy to see that both results are in qualitative agreement with each other, but the values of a represented function at the same points are different. The reasons for this discrepancy are as follows. First of all, Euler equations can't describe the mixing of gases properly because of the absence of real viscosity in these equations. Secondly, the small count of pitot tubes (26) in rake during the experiment is another reason for the discrepancy. We think that these two reasons make the CFD function more sharp than the experimental one, but averaged values must be close for both functions because of the smoothing of the picks during integration.

Comparison of the static pressure distribution along the nozzle's sidewall is shown in Fig. 11. Experimental pressure is received by the pressure taps with numbers 1–6 (Fig. 5). The Mach number of outer flow $M = 0.6$, the nozzle pressure ratio $NPR = 2.8$ (dotted line and light markers at Fig. 11 for CFD and experiment, respectively), and $NPR = 3.12$ (solid line and dark markers). The good agreement between experimental and CFD data confirms the idea that the Euler equations describe the main features of the flow after the mixer. It also explains a good agreement between experimental and CFD data for the thrust loss coefficient ($M = 0.6$), which is shown at Fig. 12. Of course, it doesn't mean that the problem is solved. The discrepancy of CFD and experimental data at $M = 0$ (Fig. 12) is because of the absence of adequate viscosity being taken into account. The data obtained in this work are the best initial information for the clearest understanding of the results (which will be received in the near future for turbulent flow), because comparing these two solutions will clarify the influence of turbulent viscosity to the flow mixing process.

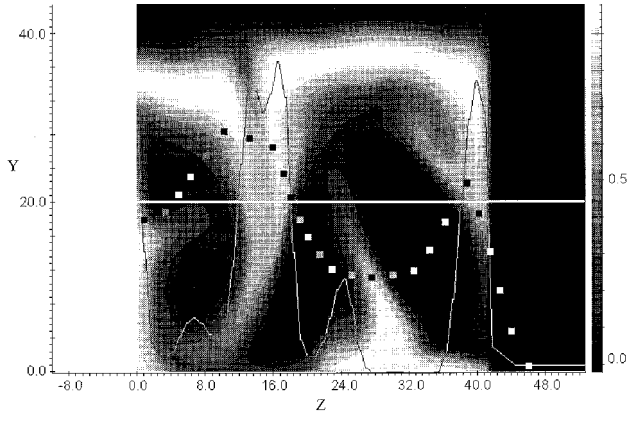

Fig. 10 Total pressure distribution at the exit section of ejector.

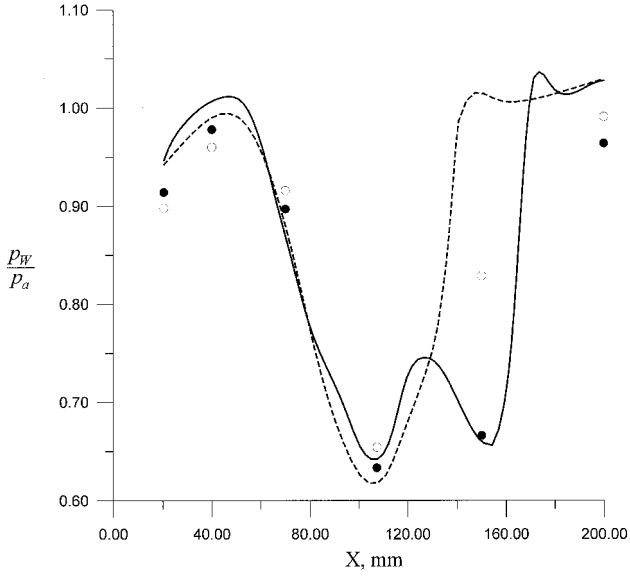

Fig. 11 Static pressure distribution along nozzle's sidewall.

Table 1 Comparison of static pressure received by pressure dots, PSP methods, and CFD

	Number of pressure dots in accordance with Fig. 5					
NPR	1	2	3	4	5	6
2.75 (taps)	0.965	0.892	0.708	0.723	0.945	1.008
2.75 (CFD)	0.909	0.929	0.867	0.907	1.012	0.977
2.75 (PSP)	——	——	0.72	0.774	0.943	1.015
4.0 (taps)	0.973	0.943	0.777	0.563	0.824	1.031
4.0 (PSP)	——	——	0.835	0.564	0.818	1.052

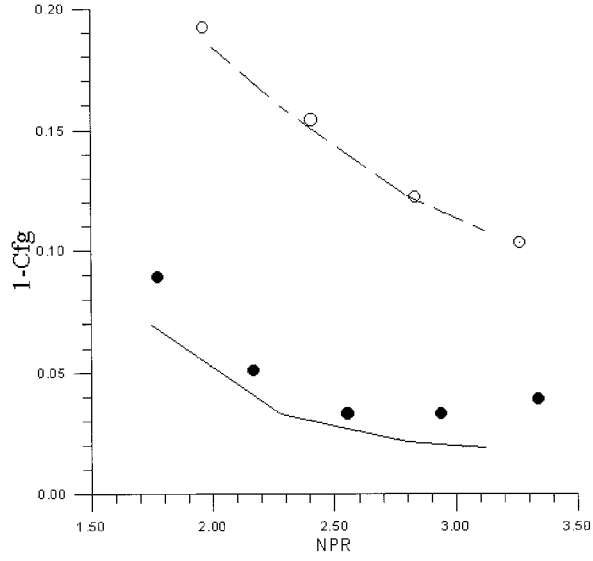

Fig. 12 Nozzle thrust losses.

Results received using PSP technology are shown in Table 1. The PSP data give good agreement with results received by means of pressure taps measurements. The discrepancy between the results of two different type experiments in the taps' points shown at Fig. 5 is not very large. It confirms the good possibility of using PSP even in such a complicated case. CFD (Euler solution) in the $M = 0$ case can't give good results and it is the subject for future investigations.

Conclusions

The first results of calculations using a model of compressible inviscid flow show that 1) the main features of the two different flow interactions in the nozzle mixer are in a good agreement with experimental data; 2) the flow in the mixer is characterized by intensive vortexes created as a result of inner and outer flow interactions; 3) the wake surface received in calculations is not smooth and looks like the Kelvin-Helmgoltz nonstability of the wake; and 4) the numerical method described in this paper can be used for the thrust losses prediction at the stage of the experiment preparation.

Acknowledgments

This investigation was supported by the International Science and Technology Center in Moscow. The authors thank S.

Matyash, who created the grid for the three-dimensional nozzle calculations, and S. Mikhailov, who prepared the postprocessor's graphics. The authors are most grateful to M. Engulatova for help in preparation of the manuscript.

References

[1]Friedrich R., "Compressible Turbulence," *2nd Space Course on Low Earth Orbit Transportation*, Vol. 1, Munich Univ. of Technology, 1993, pp. 15.1–15.45.

[2]Coakley, T. J., "Turbulence Modeling Methods for the Compressible Navier-Stokes Equations," AIAA Paper 83-1693, July 1983.

[3]Dash, S., Weilersteen, G., and Vaglio-Laurin, R., "Compressibility Effects in Free Turbulent Shear Flows," Air Force Office of Scientific Research, TR-75-1436, 1975.

[4]Godunov, S. K., Zabrodin, A. V., Ivanov, M. Y., Kraiko, A. N., and Prokopov, G. P., *Numerical Solution of Multidimensional Gas-Dynamics Tasks*, Nauka, Moscow, 1976 (in Russian).

[5]Kolgan, V. P., "Implementation of Minimal Derivative Principle for the Creation of Numerical Scheme for the Calculation of Shock Solutions of Gas-Dynamics," *Scientific Notes of TsAGI*, Vol. 3, No. 6, 1972, pp. 68–77 (in Russian).

[6]Rodionov, A. V., "Monotone Scheme of Second Order of Approximation for Marching Calculations of Non-Equilibrium Flows," *Journal of Computer Mathematics and Mathematical Physics*, Vol. 27, No. 4, 1987, pp. 585–593 (in Russian).

[7]Rodionov, A. V., "How to Rise the Approximation Order of S. K. Godunov Scheme," *Journal of Computer Mathematics and Mathematical Physics*, Vol. 27, No. 12, 1987, pp. 1853–1860 (in Russian).

[8]Harten, A., "High Resolution Schemes for Hyperbolic Conservation Laws," *Journal of Computational Physics*, Vol. 49, No. 3, 1983, pp. 357–393.

[9]Tillyaeva, N. I., "Generalization of Modified S. K. Godunov Scheme to the Arbitrary Non-regular Grids," *Scientific Notes of TsAGI*, Vol. 17, No. 2, 1986, pp. 18–26 (in Russian).

[10]Oran, E. S., and Boris, J. P., *Numerical Simulation of Reactive Flow*, Elsevier, New York, 1987.

[11]Jameson, A., "Transonic Airfoil Calculations Using the Euler Equations," *Numerical Methods in Aeronautical Fluid Dynamics*, Vol. 5, 1982, pp. 289–308.

[12]Krasheninnikov, S., Mironov, A., Pavlukov, E., Zitinev, V., Julliard, J., and Maingre, E., "An Experimental Study of 2-D Mixer-Ejector Noise and Thrust Characteristics," AIAA Paper 96-1668, May 1996.

[13]Kaji, S., and Sugimura, K., "Flow and Acoustics of a Mixer-Ejector Nozzle for Jet Noise Suppression," 4th International Congress on Sound and Vibration, St. Petersburg, Russia, June 1996.